**Atmospheric
Chemistry
and Physics
Discussions**

Photoacoustic optical properties at UV, VIS, and near IR wavelengths for laboratory generated and winter time ambient urban aerosols

M. Gyawali[1], W. P. Arnott[1], R. A. Zaveri[2], C. Song[2], H. Moosmüller[3], L. Liu[4], M. I. Mishchenko[4], L.-W. A. Chen[3], M. C. Green[3], J. G. Watson[3], and J. C. Chow[3]

[1]Physics Department, University of Nevada, Reno, Nevada System of Higher Education, 1664 N. Virginia Street, Reno, NV, 89557, USA
[2]Atmospheric Sciences and Global Change Division, Pacific Northwest National Laboratory, Richland, WA, 99352, USA
[3]Desert Research Institute, Nevada System of Higher Education, 2215 Raggio Parkway, Reno, NV, 89512, USA
[4]NASA Goddard Institute for Space Studies, 2880 Broadway, New York, NY 10025, USA

Correspondence to: M. Gyawali (madhug@unr.edu)

ACPD

11, 25063–25098, 2011

Photoacoustic optical properties

M. Gyawali et al.

Title Page

Abstract	Introduction
Conclusions	References
Tables	Figures

Back | Close

Full Screen / Esc

Printer-friendly Version

Interactive Discussion

Abstract

We present the first laboratory and ambient photoacoustic (PA) measurement of aerosol light absorption coefficients at ultraviolet (UV) wavelength (i.e. 355 nm) and compare with measurements at 405, 532, 870, and 1047 nm. Simultaneous measurements of aerosol light scattering coefficients were achieved by the integrating reciprocal nephelometer within the PA's acoustic resonator. Absorption and scattering measurements were carried out for various laboratory-generated aerosols, including salt, incense, and kerosene soot to evaluate the instrument calibration and gain insight on the spectral dependence of aerosol light absorption and scattering. Exact T-matrix method calculations were used to model the absorption and scattering characteristics of fractal-like agglomerates of different compactness and varying number of monomers. With these calculations, we attempted to estimate the number of monomers and fractal dimension of laboratory generated kerosene soot. Ambient measurements were obtained in Reno, Nevada, between 18 December 2009, and 18 January 2010. The measurement period included days with and without strong ground level temperature inversions, corresponding to highly polluted (freshly emitted aerosols) and relatively clean (aged aerosols) conditions. Particulate matter (PM) concentrations were measured and analyzed with other tracers of traffic emissions. The temperature inversion episodes caused very high concentration of $PM_{2.5}$ and PM_{10} (particulate matter with aerodynamic diameters less than 2.5 μm and 10 μm, respectively) and gaseous pollutants: carbon monoxide (CO), nitric oxide (NO), and nitrogen dioxide (NO_2). The diurnal change of absorption and scattering coefficients during the polluted (inversion) days increased approximately by a factor of two for all wavelengths compared to the clean days. The spectral variation in aerosol absorption coefficients indicated a significant amount of absorbing aerosol from traffic emissions and residential wood burning. The analysis of single scattering albedo (SSA), Ångström exponent of absorption (AEA), and Ångström exponent of scattering (AES) for clean and polluted days provides evidences that the aerosol aging and coating process is suppressed by strong

temperature inversion under cloudy conditions. In general, measured UV absorption coefficients were found to be much larger for biomass burning aerosol than for typical ambient aerosols.

1 Introduction

Atmospheric aerosols impact air quality and Earth's radiation balance. Aerosol light scattering redistributes electromagnetic energy in the atmosphere, whereas light absorption transforms it into thermal energy by heating absorbing aerosols and their surroundings. The absorption and scattering coefficients of aerosol are needed for modeling atmospheric radiation transfer (Clarke et al., 1987). These quantities are challenging to quantify and are associated with large uncertainties in the radiative forcing (Bergstrom et al., 2007; Bergstrom et al., 2009). Aerosol optical properties depend on particle size, morphology, refractive index (RI), and wavelength of electromagnetic radiation and must be specified over the entire solar spectrum (Levoni et al., 1997).

Carbonaceous aerosols account for much of the atmospheric particulate matter mass that affects incoming solar radiation via scattering and absorption (Sun et al., 2007). These aerosols consist of two major components: elemental carbon (EC), also defined as black carbon (BC) or "soot", and organic aerosol (OA) (Seinfeld and Pandis, 2006). BC is emitted as a result of incomplete combustion of carbon-rich fuels. The other component, OA, though present in much higher mass concentrations than BC for ambient samples, is more elusive as its origins as well as optical and chemical properties vary greatly with source, transformation, and sink (D'Alessio et al., 1998). OA exhibits many molecular forms that have different physical and chemical properties and often exists independently of BC (Jacobson et al., 2000). The OA that is directly emitted from combustion or biogenic processes is referred to as primary organic aerosol (POA). OA is also formed in-situ through the oxidation of gaseous organic precursors that transfer to the aerosol phase by condensation or nucleation, referred to as secondary organic aerosol (SOA). SOA formation involves two processes: gas-phase

chemical transformation and change of phase. Photochemical transformation also promotes inorganic aerosol formation.

BC strongly absorbs throughout the entire solar spectrum (Horvath, 1993; Moosmüller et al., 2009). The refractive index (RI) of BC depends predominantly on fuel type, combustion phase, degree of graphitization, and atmospheric processing (Andreae and Gelencsér, 2006; Bond and Bergstrom, 2006). Pure carbon (i.e. graphitic state) has RI as large as 2 +1i, where the real and imaginary parts of RI impact both light scattering and absorption. The formation of BC through pyrolysis of hydrocarbon fuels is a complicated process. This process leads to the formation of complex substances like oils, tars, and solids, while the adsorption and continuing elimination of hydrogen at higher temperature results in an increase in crystal size and graphitization of the fuel (Grisdale, 1953). For instance, diesel soot appears as an onion-shell structure of nano crystalline graphite having domain sizes of 2–3 nm (Wentzel et al., 2003). Out of the four valence electrons of carbon atoms in graphite, three are in the hybrid sp^2 state and one is in the p state. The electrons in the hybrid state form σ bonds and those in the p state form π bonds due to the mutual overlapping above and below the graphitic plane, and become delocalized (Bond and Bergstrom, 2006). Electrons in the π bond can move rather freely and absorb electromagnetic radiation from at least the ultraviolet (UV) to the near IR. Electrons in σ bonds are effective in UV absorption.

While BC aerosols absorb strongly over the entire solar spectrum, some OA absorbs efficiently in the UV and blue regions (Barnard et al., 2008; Bergstrom et al., 2007; Bond, 2001; Chakrabarty et al., 2010; Jacobson, 1999; Kirchstetter et al., 2004; Martins et al., 2009; Roden et al., 2006). These organic materials appear yellowish/brownish and are known as "brown carbon" (Andreae and Gelencsér, 2006). Brown carbon is commonly found in secondary and biomass burning aerosols (e.g. Andreae and Gelencsér, 2006; Chakrabarty et al., 2010; Chen et al., 2010). UV radiation encompasses only 10 % of the total solar irradiance, so details of its direct radiative forcing are often ignored in climate modeling (Corr et al., 2009). There have been many investigations of aerosol optical properties in the visible spectrum, though in situ mea-

Title Page

Abstract | Introduction

Conclusions | References

Tables | Figures

◄ | ►|

◄ | ►

Back | Close

Full Screen / Esc

Printer-friendly Version

Interactive Discussion

surements of UV absorption by ambient aerosols are rare (Kikas et al., 2001; Taylor et al., 2008).

Radiative transfer in the UV with respect to photochemistry has motivated us to develop a new photoacoustic instrument and nephelometer that can measure in situ
5 aerosol absorption and scattering coefficients at UV wavelengths. UV radiation is the dominant driver of atmospheric chemistry. The photo dissociation of gaseous species due to UV radiation is responsible for smog and ozone formation in the troposphere (Jacobson, 1999). Most photolysis is due to UV radiation between 290 to 420 nm (Hofzumahaus and Kraus, 2002). Jacobson (1999) found that the nearly 50 % decline
10 in UV radiation within the boundary layer (BL) in Los Angles was due to substantial UV absorption by nitrated and aromatic aerosols and gaseous species. A very recent study indicated nighttime formation of particulate organic nitrate and organosulfate species in coal-fired power plant plumes (Zaveri et al., 2010) that may also absorb UV radiation the following day.

15 This study reports multispectral photoacoustic absorption and scattering measure-ments at wavelengths 355, 405, 532, 870, and 1047 nm for laboratory-generated aerosol as well as for ambient aerosol during the months of December 2009 and Jan-uary 2010. The hourly concentrations of $PM_{2.5}$ and PM_{10} and gaseous pollutants (CO, NO, and NO_2) are also analyzed for the same period. The simultaneous measurement
20 of aerosol optical properties at multiple wavelengths provides an improved coverage of the solar spectrum and offers a way to single out the spectral signature of BC and OA aerosols. Nevertheless, our previous investigation (Gyawali et al., 2009) suggests that even non-absorbing coatings on BC can be disguised as "brown carbon" or light ab-sorbing OA, so it is not always possible to separate the effects of coatings on amplifying
25 aerosol absorption and intrinsic absorption by the coating (Jacobson et al., 2000).

2   Laboratory generated aerosols and T-matrix calculations

2.1   Laboratory generated aerosols

This section presents the absorption and scattering coefficients measured for three different types of laboratory-generated aerosols. These include strongly scattering salt (NaCl) aerosol, strongly absorbing kerosene soot aerosol, and short-wavelength absorbing incense aerosol. Use of these aerosols under laboratory circumstances allows for the evaluation of the instrument's performance and accuracy. The details of the working principle of the PA instrument as well as the use of the salt and kerosene soot aerosols to achieve scattering and absorption calibration at 355 nm can be found in the supplement. Besides functioning as instrument performance tests, these measurements provide an opportunity for the analysis of the wavelength dependence of absorption and scattering for a range of aerosols that might be representative of atmospheric aerosols in different locations and during different events.

Incense is used to produce fragrances for ceremonial purposes and in residential homes. A wide variety of substances are used to produce incense, including wild flowers, strawberries, sandal wood and other aromatic woods, and resins. Burning incense produces mostly organic compounds including polycyclic aromatic hydrocarbons (PAHs), aromatic aldehydes, and aliphatic aldehydes, with a particle mass median aerodynamic diameter ranging from 150 to 300 nm (Ji et al., 2010; Yang et al., 2007). The incense used for this study was manufactured in India by coating the pulverized wooden materials and other ingredients on a supporting wooden core and had brown color. One incense stick was ignited in a chamber and the flame was immediately extinguished to obtain smoke from the smoldering phase. Incense is a good aerosol source that has strong absorption at shorter wavelengths due to brown carbon and can be used as surrogate for smoldering biomass combustion.

Kerosene soot aerosol has been employed extensively in the laboratory to calibrate the PA absorption measurements, to evaluate the measurements and precision of aerosol light absorption measuring instruments, and to study the aerosol absorption

and scattering in external and internal mixing states (Arnott et al., 2000, 2005; Petzold et al., 2005; Sheridan et al., 2005). It is a surrogate for diesel soot and exhibits nearly inverse wavelength dependence of the aerosol light absorption coefficient (Sheridan et al., 2005).

2.1.1 Calculation of Ångström exponent of absorption (AEA), Ångström exponent of scattering (AES) and single scattering albedo (SSA)

AEA is used to analyze the spectral dependence of aerosol light absorption, to characterize the aerosol composition, and to model aerosol radiative forcing. The aerosol light absorption at a single wavelength can be extrapolated to other wavelengths by a power law relationship as

$$\beta_{abs}(\lambda) = C^* \lambda^{-\alpha_{abs}}, \tag{1}$$

where $\beta_{abs}(\lambda)$ is the aerosol absorption coefficient at the wavelength λ of the light, C is a constant independent of wavelength, and α_{abs} is the AEA. The AEA, $\alpha_{abs}(\lambda_1, \lambda_2)$ can be calculated from the aerosol light absorption coefficient measured at two different wavelengths λ_1 and λ_2 as (Moosmüller et al., 2011)

$$\alpha_{abs}(\lambda_1, \lambda_2) = \frac{\ln\left(\beta_{abs}(\lambda_1)/\beta_{abs}(\lambda_2)\right)}{\ln(\lambda_2/\lambda_1)} \; . \tag{2}$$

For small size parameter, absorbing spherical particles with a wavelength independent refractive index, AEA = 1 (Moosmüller and Arnott, 2009; van de Hulst, 1981).

The Ångström exponent of scattering (AES) is used to characterize aerosol size. Like AEA, AES is also a power law relationship and can be calculated as the Eqs. (1) and (2) by using aerosol scattering coefficients (β_{sca}). The magnitude of AES approaches a value of 4 for small particles and approaches 0 for large particles with a wavelength-independent refractive index (Bohren and Huffman, 1983). Another calculated optical

property is the single scattering albedo (SSA), which is defined as the ratio of scattering coefficient β_{sca} to the extinction coefficient, $\beta_{\mathrm{abs}} + \beta_{\mathrm{sca}}$ as

$$\mathrm{SSA} = \frac{\beta_{\mathrm{sca}}}{\beta_{\mathrm{sca}} + \beta_{\mathrm{abs}}}. \tag{3}$$

Power law relationships, Eqs. (1) and (2), were used to calculate AEA and AES to study the spectral variations of these quantities for laboratory aerosol and are plotted in Fig.1a. The value of AEA is 0.80 for kerosene and 4.52 for incense aerosols. The data shows a curvature of the incense absorption coefficients as a function of wavelength, resulting in a larger AEA for shorter wavelengths than for longer ones. Such a curvature has previously been described for AERONET extinction (Schuster et al., 2006), and for brown carbon absorption coefficients using a damped simple harmonic oscillator model (Moosmüller et al., 2011). Further, β_{abs} for incense aerosol at 355 nm was found to be nearly 20 times higher than the IR β_{abs} at 870 nm. Kerosene soot is a good example of black carbon while incense aerosol is a brown carbon example. Similarly, AES is 1.8 for kerosene soot and 2.0 for incense aerosols, indicating larger aerosol size for kerosene soot aerosol than for incense aerosol. Figure 1b compares SSA for kerosene soot and incense burning aerosols. SSA decreases with wavelength for kerosene soot yet it increases for incense burning aerosol with wavelength, yielding positive and negative Ångström exponents of SSA (AESSA), respectively (Moosmüller and Chakrabarty, 2011). Incense smoke behaves optically similar to primary emissions from biomass burning that have a large OC fraction (Lewis et al., 2008).

2.2 T-matrix calculations of spectral light absorption by black carbon

This section presents the T-matrix calculations to explore the parameter space for intensive optical properties: SSA, AEA, and AES. The laboratory-measured values of SSA, AEA, and AES for kerosene soot were compared with the corresponding T-matrix calculations at 405 and 870 nm and we attempted to estimate the number of monomers (N) and fractal dimension (D_f) for the closure study.

Title Page

Abstract | Introduction

Conclusions | References

Tables | Figures

◄ | ►

◄ | ►

Back | Close

Full Screen / Esc

Printer-friendly Version

Interactive Discussion

During incomplete combustion of hydrocarbon fuel, freshly emitted BC particles commonly are fractal-like chain aggregates of spherules. The fractal structure of the aggregates can be described by the following mathematical scaling relation (Chakrabarty et al., 2006; Liu et al., 2008; Sorensen, 2001):

$$N = k_0 \left(R_g / a \right)^{D_f} \tag{4}$$

where k_0, a, and R_g are fractal prefactor, monomer radius, and radius of gyration, respectively. The monomer radius a commonly ranges between 10 and 25 nm (Bond and Bergstrom, 2006). D_f describes the compactness of aggregate morphology. It is closer to 3.0 for densely packed spherical aggregates, and closer to 1 for near-linear chain-like aggregates. The prefactor k_0 is additionally related to the level of compactness of the aggregates (Sorensen and Roberts, 1997).

The T-matrix method is a numerically exact and efficient solution to Maxwell's equations applicable to a wide range of particles (Mackowski and Mishchenko, 1996; Mackowski, 2006; Mishchenko et al., 1996). Most importantly, it can be applied to obtain scattering and absorption coefficients for homogeneous (i.e. uncoated) fractal-like soot aggregates with no approximation. Particle position coordinates, size parameters, and RI are the input parameters for the T-matrix calculation, whereas scattering and absorption cross sections are output parameters. The position coordinates are generated using cluster-cluster aggregation (Mackowski, 2006) for a given D_f, N, and k_0 value. In our study, we adopted $a = 15$ nm, and RI = 1.75+0.5i at both wavelengths, as used in previous work (Liu et al., 2008). Figure 2a and b show the variation of the SSA at 870 and 405 nm versus D_f, for various N (i.e. 200, 400, 600 and 800). The plots show that SSA at both wavelengths increases more quickly with D_f for $D_f > 2.0$ and also depends on N. T-matrix calculations indicate that, as fractal aggregates become more and more compact with the atmospheric aging process (Lewis et al., 2009), their SSA increases even in the absence of additional non-absorbing material. Figure 2c and d are the similar plots for AES and AEA. For fixed monomer diameter both AES and AEA decrease continuously with increasing D_f. The value of AEA is about 1.05 for all monomers at

Photoacoustic optical properties

M. Gyawali et al.

Title Page

Abstract | Introduction

Conclusions | References

Tables | Figures

|◄ | ►|

◄ | ►

Back | Close

Full Screen / Esc

Printer-friendly Version

Interactive Discussion

$D_f = 1.25$ (open fractal aggregates). As fractal aggregates become more compact, the variation of both AES and AEA is quite different depending upon N. For D_f around 3.0, AEA ranges from 1.04 for $N = 200$ to 0.69 for $N = 800$. The scattering cross-section and SSA of the soot aggregates increase continuously with the compactness of the aggregates (Liu et al., 2008). However, the absorption cross-section might increase or decrease with D_f depending upon the dominance of interaction among the spherules and the shielding effect due to the compactness of the aggregates (Liu et al., 2008).

AEA could decline due to the change to a more compact spherical shape of the freshly emitted fractal aggregates as a result of coating, aging, and photochemical activity in the atmosphere. The extent of coating and the core size also determine the absorption enhancement (Lack et al., 2009). The arrows on the plots (Fig. 2a and b) indicate the inferred values of D_f around 2.06 at $N = 200$ by using laboratory measurements of SSA, and D_f around 2.62 at $N = 800$ by using laboratory measurements of AES and AEA, and T-matrix calculation (Fig. 2c and d). However, by moving along the D_f axis we can find multiple possible solutions for N. The optical properties of fractal-like soot aggregates are the complex functions of RI, N, D_f and a as described by Liu et al. (2008). This implies that more information on particle size including coating and mixing state is needed to confidently indentify either D_f or N for the laboratory generated kerosene soot.

3 Ambient measurements

3.1 Meteorological conditions and classification of measurement events

In this study, we used meteorological data from http://www.wrcc.dri.edu/rcc.html and balloon soundings from http://weather.uwyo.edu/upperair/sounding.html pertaining to the Reno area. The data were analyzed from 18 December 2009 to 18 January 2010 to study the enhancement of β_{sca} and β_{abs} by freshly emitted traffic and wood burning aerosols trapped near the surface due to temperature inversion. Temperature gen-

erally decreases with altitude in the lower part of the atmosphere, but during certain meteorological situations, the surface may become colder than the air at higher elevations, leading to temperature inversion conditions, which tend to suppress the vertical mixing of air. During temperature inversion periods, the local health officials of Washoe County, Nevada announced air pollution alerts to encourage inhabitants to refrain from extended outdoor activities, and banned residential wood burning (see, http://www.co.washoe.nv.us/health/pr/pr.html). The β_{abs} during these conditions was comparable to that of the California wild fire season in the summer of 2008 and pollution in Mexico City (Gyawali et al., 2009; Paredes-Miranda et al., 2009). Figure 3 presents the aerosol time-series of β_{sca} and β_{abs} at 355 nm in conjunction with meteorological parameters from two near surface stations in Reno separated by an altitude difference of 143 m. Figure 3a and b display the temperature gradient normalized by the dry adiabatic lapse rate ($-9.8\,°C\,km^{-1}$) and the wind speed, respectively. Large negative values of the normalized temperature gradient indicate the strength of the temperature inversion. The balloon soundings were at the NWS office (near DRI) and are launched from an elevation about 150 m above the valley floor. Thus the higher than valley floor balloon launch site may underestimate the inversion strength. The relatively high wind speed of 6 to 7 m s^{-1} breaks the temperature inversion on January 12. Figure 3c shows the temperature profiles from the morning balloon soundings for major temperature inversion events. Additional short-term temperature inversion of a similar nature took place during December and January. Figure 3d displays the two-minute average time-series of β_{sca} and β_{abs} at 355 nm. Four episodes of elevated β_{sca} and β_{abs} are centered around 19, and 25 December 2009, and 6 and 16 January 2010, and are associated with temperature inversion and diminished wind speed (as shown in Fig. 3a, b, and c). These high pollution episodes were predominantly of local origin, with air trapped in the lower levels due to severe stagnation. Results presented here show that the 355 nm β_{sca} and β_{abs} of trapped emissions can be ten times greater than those for clean days. For such polluted days, the increased UV extinction slows down the formation of SOA and ozone (Barnard et al., 2008).

Based upon the meteorological parameters and the magnitude of β_{sca} and β_{abs}, we have classified the measurements made from 18 December to 18 January into two groups: "clean days" and "polluted days." Days were classified as polluted days if the average β_{abs} values at 355 nm for the particular days were about 40 Mm^{-1} or higher, such as for 18 to 20, 24 to 26, and 31 December, 4 to 6 and 15 and 16 January. The PM$_{2.5}$ mass concentration during the polluted days was at least 40 µg m^{-3} (air quality public warning "Sensitive") or as high as 90 µg m^{-3} (air quality public warning "Unhealthy"; see, http://alg.umbc.edu/usaq).

3.2 Particulate matter (PM) and gaseous pollutant concentrations

This section presents particulate matter (PM) and gaseous pollutant concentrations from an air quality monitoring station (South of the Truckee River, EPA ID#32-031-0016), ∼0.9 miles distance from the Department of Physics, University of Nevada, Reno, USA, where the aerosol optics measurements were made. Hourly at PM$_{2.5}$ and PM$_{10}$ mass concentrations were measured by Beta Attenuation Monitor (BAM) (MetOne SASS), whereas the Federal Reference Method (FRM) was used for 24-h speciation of PM$_{2.5}$ mass concentrations and additional instruments measured concentrations of gaseous pollutants. The operation of the BAMs has been described in detail elsewhere (Chow et al., 2006; Huang and Tai, 2008; Schwab et al., 2006; Takahashi et al., 2008). In brief, BAMs draw air through a size-selective inlet, then through a quartz-fiber filter tape. A radioactive source, usually low-level carbon-14, generates a stream of electrons (beta rays) through the sample spot as the particle deposit accumulates. As the filter spot loads up, the penetrated electron count decreases, and the decrease is proportional to the sample loading. The filter tape can be set to advance every hour, or to advance when it reaches a selected mass loading. The working principle of FRM is described in BGI (2009a, b). In brief, PM$_{2.5}$ is collected on 47 mm PTFE membrane media at a volumetric sample rate of 16.67 lpm after being size discriminated through two US EPA designed inertial separators. Ambient temperature and barometric pressure measurements are made at actual sample conditions. A micro-

processor and sophisticated volumetric flow control system are integrated to maintain precise sampling parameters while sampling data are continuously logged into the processor memory. Five minute actual ambient temperature and pressure conditions with volumetric sample flow rate, filter temperature, and pressure are recorded.

Diurnal concentrations of CO, NO, NO_2, O_3, $PM_{2.5}$, and coarse particles (PM_{10}–$PM_{2.5}$) averaged for clean days and polluted days are shown in Fig. 4. For CO and NO, the maximum values occurred during the morning rush hours, followed by a decrease in those quantities in the late morning due to dilutions of these pollutants and growth of the BL. The concentrations increased again because of the evening rush hours and the decrease of the BL. The peak of the NO_2 concentration is generally delayed relative to the other gaseous pollutant concentration. The O_3 concentrations increased rapidly from late morning as a result of reactions involving other pollutants including NO_2, but the peak concentrations occurred in the late afternoon. The photochemical reactions that create ozone generally require intense sunlight and warm air temperatures. $PM_{2.5}$ and coarse particle mass concentrations did not increase significantly during the morning and evening rush-hours.

The temperature inversions resulted in high concentrations of PM and gaseous pollutants besides O_3, as shown in Fig. 4. Our study corroborates other reports where higher levels of O_3 have been reported during non-inversion days (Janhall et al., 2006). O_3 has lower concentrations during polluted days because the trapped NO in the inversion layers reacts with O_3 to form NO_2 as found by Janhall et al. (2006). Another possible explanation for the lower concentration of O_3 might be due to the reduced mixing of aloft O_3 and its precursors during temperature inversions (Chen et al., 2002). $PM_{2.5}$ and coarse particle concentrations exhibited much higher concentrations with pronounced diurnal variation during polluted days. $PM_{2.5}$ primary emissions are likely influenced by traffic and residential wood combustion (Watson and Chow, 2002). The mid-day peaks of $PM_{2.5}$ and coarse particles, however, may result from the temporal overlap between the evening rush hour, the secondary aerosol produced during day time, wind-related dust, and traffic resuspension (Stephens et al., 2008).

Figure 5 shows 24 h averages of $PM_{2.5}$ component mass concentrations for highly polluted days (18 and 24 December and 5 January) and relatively clean days (21 December, and 14 and 17 January). The comparison shows slightly higher concentrations of organic material, much higher quantities of ammonium nitrate (NH_4NO_3), and
5 a higher amount of unexplained mass during the polluted days. The unexplained mass highly correlates with the NH_4NO_3. Furthermore, NH_4NO_3 was the primary cause of the lift in the $PM_{2.5}$ mass concentrations over the $35\,\mu g\,m^{-3}$ threshold during polluted days. Nitric acid (HNO_3) is formed from oxidation of NO_x (NO_2 + NO) via either photochemical or nighttime reactions (Watson and Chow, 2002). NH_4NO_3 is formed from
10 the reaction of HNO_3 and ammonia (NH_3) from agricultural activities. In addition, there is a possibility of the formation of organic nitrates in the presence of nitrates and organic species in pollution plumes (Flowers et al., 2010). Particle phase organic nitrates are strong absorbers at UV wavelength (Jacobson, 1999). The strength of the absorption increases with the acidity of organic nitrates. However, consistently low values
15 of AEA (i.e. less than 1.2) for all pairs including the analysis of multispectral β_{sca} and β_{abs} (presented in the next section) does not support the presence of short wavelength absorbing acidic organic species during polluted days.

3.3 Ambient aerosol optical properties measurements

In this section, we present our findings on diurnal variation of half-hour average ambient
20 extensive and intensive aerosol optical properties at wavelengths of 355, 405, 532, and 870 nm from 18 December 2009, to 18 January 2010. These measurements were obtained at the Physics building of the University of Nevada, Reno, USA. PA sampled from an inlet at a flow rate of ∼3 lpm through a ∼3 m insulated copper inlet line located ∼10 m above the ground. Spectral and diurnal variations of β_{sca}, β_{abs}, AES, AEA,
25 and SSA during the study periods were analyzed and classified for "clean days" and "polluted days".

3.4 Spectral and diurnal variations of β_{sca} and β_{abs}

Figure 6a and b compare the diurnal and spectral variations of half-hour averages of β_{sca} during clean days and polluted days, respectively. These data describe common effects of the BL dynamics, day-time photochemical activity, and additional formation of non-light absorbing particles. Similarly, Fig. 6c and d compare the β_{abs} measurements. In comparison, peak values of β_{sca} and β_{abs} on stagnant days are nearly twice as large as those values measured on clean days. This can be attributed to the increased concentration of PM, specifically ammonium nitrate, soot, and organics during the polluted days. Additionally, during polluted days the peak of the scattering coefficient was 4 h later than the absorption coefficient peak possibly due to gas to particle formation of secondary aerosol that scatters light effectively, as previously seen in Mexico City (Paredes-Miranda et al., 2009).

Aerosol extinction at near UV wavelengths is of considerable importance for photochemical processes, for example for the photolysis of NO_2 and its relation to the ozone production cycle. In addition, gas to particle conversion by UV radiation produces PM that affects the planetary radiation budget (Reuder and Schwander, 1999).

3.4.1 Spectral and diurnal variation of SSA

SSA is a crucial optical parameter for determining the sign of net radiative forcing by aerosol. The value of 0.85 represents an approximate boundary point. Values above 0.85 generally represent a cooling impact while values less than this quantity represent an heating impact (Hansen et al., 1981). While the temporal and spatial variations of SSA in the atmosphere are associated with BL mechanisms, rush hour activity, and other natural and anthropogenic events, the spectral variations of SSA are dependent on aerosol size, chemical composition, and mixing state. For dust and biomass burning aerosols that absorb significantly at shorter solar wavelengths, SSA generally increases with wavelength, while this tendency reverses for small-particle BC aerosol from vehicular exhaust (Bergstrom et al., 2002; Gyawali et al., 2009; Sokolik and Toon,

1999). Figure 6e and f show the diurnal and spectral changes in half-hour average of SSA computed with Eq. (3). The role of temperature inversion on the diurnal evolution of aerosol size and composition is reflected in the magnitude of SSA. Minimum SSA is observed around 09:00 LT, coincident with morning peak traffic, while maximum SSA is observed at 15:00 LT, concurring with the low value of AES and dominance of larger particles as evidenced in Fig. 4a and b. Compared to the other wavelengths, diurnal half-hour SSA at 355 nm has the highest value, varying from 0.80 to 0.92. Other wavelengths exhibit a distribution from 0.65 at 870 nm to 0.88 at 532 nm. Polluted days show less diurnal variation and lower values of SSA due to the averaging effects of multiple days of stagnation.

Though our measurement techniques and approaches are for aerosol sampled close to ground level, it is worthwhile to compare our findings with other published data even if these data are mainly based on remote sensing and focus on the total atmospheric column. Since SSA is an intensive parameter, for well-mixed conditions in-situ ground based and remote sensing measurements should have a similar relationship. Hofzumahaus et al. (2002) applied the best fit of modeled actinic fluxes to spectroradiometer measurements and came up with 0.87 and 0.95 for SSA at 355 nm for different days in Greece. Corr et al. (2009) found SSA variations from 0.73 to 0.85 at 368 nm using a multifilter rotating shadowband radiometer (MFRSR) in Mexico City. Barnard et al (2008) reported SSA = 0.80 at 368 nm using a UV-MFRSR technique. These authors have also reported SSA for visible wavelengths and acknowledged that the observed lower value towards the UV region, when present, is due to the enhanced absorption by certain organic compounds in aerosols.

3.4.2 Spectral and diurnal variation of AES

The wavelength dependence of AES has been used to understand the dominant aerosol size distribution along with the optical properties of biomass burning, urban, and desert dust aerosols (Eck et al., 1999; Reid et al., 1999). Dubovik et al. (2002) described values of Ångström exponent of extinction (AEE) varying from −0.1 to 2.5

to identify aerosol sources including desert dust and biomass burning in their comprehensive survey of aerosol optical properties at locations around the globe (Dubovik et al., 2002). Values of AEE close to 0 occur when the scattering is dominated by large dust particles, and AEE close to 2.5 represents smoke particles. These values were reported from ground-based Sun photometer remote sensing measurement techniques.

Figure 7a and b present the variations of AES during the clean and polluted days. $\beta_{sca}(\lambda)$ was used in Eq. (2) for the calculations of AES, where 870 nm was taken as the reference wavelength. Values of AES are large in the early morning, with AES = 1.8 for the 355/870 nm pair, and around 1.3 for longer-wavelength pairs (405/870 and 532/870 nm), a widely used value for the atmosphere of natural composition. On clean days, AES values for the longer-wavelengths pairs decline continuously after midnight and are at their minimum value of ~0.8 about four hours after the local noon, at the warmest, most diluted time of the day. The minimum on polluted days occurs six hours after local noon, corresponding to peak particle size. In comparison, AES varies more for all pairs on wavelengths for clean days than on polluted days. The significant diurnal change of AES implies a distinct diurnal cycle for particle size. The size of the freshly emitted particles increases over their atmospheric residence time due to the various phenomena present in atmospheric processing (Reid et al., 1998). As stated above, AES is at its minimum in the later part of the day, indicating the dominance of larger particles as found in the diurnal variations of particulate matters. Turbulent mixing at the BL thickness peak may enhance coagulation, and repeatedly expose aerosol and precursors to strong UV radiation at the top of the BL. The BL expansion, photo-oxidation, condensation, and coagulation processes smear out the dominance of freshly emitted sub-micron particles, shifting to the dominance of larger-sized aged aerosol as implied in the diurnal variation of AES and measurements of $PM_{2.5}$ and coarse particle mass concentrations.

The minimum of AES for the longer-wavelength pairs occurs two hours later than for clean days, likely as a result of the delay in photo-chemically driven condensational growth of primary aerosols on polluted days. The explanation for the vastly different

Photoacoustic optical properties

M. Gyawali et al.

Printer-friendly Version

Interactive Discussion

behavior of AES for the wavelength pair, 355/870 nm, is currently unknown but maybe related to significant changes in refractive indices of different PM components between the visible (i.e. 405 and 532 nm) and the UV (i.e. 355 nm).

3.4.3 Spectral and diurnal variation of AEA

AEA responds to the composition, size, and the presence of coatings on aerosol. Recent analysis shows that AEA can be as high as 1.6 even with non-absorbing coatings on BC (Gyawali et al., 2009; Lack and Cappa, 2010). It has been shown that the core size, coating thickness, and complex refractive index of both components play a vital role in the spectral coating enhancement of absorption.

The diurnal variation of AEA is shown in Fig. 7c and d. The diurnal variations at wavelength pairs 355, 870, and 405, 870 nm exhibit similar behavior, displaying higher values in the early morning and then decreasing by noon and increasing thereafter. The value of AEA at 355, 870 nm is as high as 1.4 on clean days during nighttime hours due to biomass burning. For the wavelength pair 532, 870 nm AEA is close to one during clean days and has little variation, but remains around 0.8 during polluted days.

AEA depends on the wavelength pair as well as the mixing and coating state of the aerosols. Depending upon the nature of light absorbing OA or brown carbon, its mass absorption coefficients towards UV is significantly higher (as high as $12\,m^2\,g^{-1}$ at 350 nm) than at mid visible regions (Barnard et al., 2008; Lack and Cappa, 2010). Hence, 355 and 405 nm absorption is due to OA and BC, whereas 532 and 870 nm absorption is mainly due to BC. The maximum AEA was found around 1.4 for the pair 355, 870 nm and it can be attributed to the presence of OA from wood burning. This value decreases to around 1.0 during morning rush hour when BC emissions from vehicles are dominant. After noon, the increase in AEA for all pairs is due to the atmospheric processing of aerosols, in which coating, mixing, and coagulation are taking place. We did not observe dramatic variation of AEA for the 355/870 nm pair compared with the 405/870 nm pair. On the other hand, it is interesting to see (Fig. 7d)

that AEA remains nearly constant throughout the day. Restrictions against residential wood burning on polluted days may also result in lower AEA values at night than on clean days.

Figure 8a and b show the variation of AES and AEA at 355 and 532 nm with SSA at 355 and 532 nm, respectively. Like SSA, values of AEA are generally larger and more scattered during clean days. Even though the error bars are overlapping or touching in most of the cases, there is the clear distinction between the mean values of intensive aerosol optical properties, i.e. AES, AEA, and SSA for clean days and polluted days (Fig. 8c, d, and e). For instance, the mean values of SSA are $SSA_{polluted}^{355\ nm} = 0.83 \pm 0.02$, $SSA_{clean}^{355\ nm} = 0.87 \pm 0.02$, and $SSA_{polluted}^{870\ nm} = 0.72 \pm 0.03$, $SSA_{clean}^{870\,nm} = 0.81 \pm 0.03$, and of AEA are $AEA_{clean}^{355/870\ nm} = 1.14 \pm 0.12$, $AEA_{polluted}^{355/870\ nm} = 1.03 \pm 0.09$, and $AEA_{clean}^{532/870\ nm} = 1.0 \pm 0.05$ and $AEA_{polluted}^{532/870\ nm} = 0.78 \pm 0.04$, respectively.

4 Summary and conclusions

A new photoacoustic instrument measuring aerosol light absorption and scattering at 355 nm was constructed to explore aerosol optical properties in the UV region and to investigate light absorbing organic aerosols. Multispectral photoacoustic measurements of laboratory-generated and ambient aerosols were performed in Reno, Nevada, to evaluate the aerosol light absorption and scattering from near UV to near IR. Particulate matter, gaseous pollutants, and meteorological data in combination with aerosol optical properties were used to get insights into the winter-time urban aerosol evolution and composition. Based upon these analyses, the measurement period, from 18 December 2009 to 18 January 2010, has been divided into "polluted days" (temperature inversion) and "clean days" (well-mixed air).

The results lead to the following remarks and conclusions. The AEA is very large for incense (i.e. 4.53) compared with kerosene soot (i.e. 0.80), highlighting its use

as a surrogate for smoldering phase biomass combustion. The higher mass concentrations of $PM_{2.5}$ and coarse particles were associated with the intense ground level temperature inversions. However, O_3 concentrations were found to be higher during clean days than polluted days. The temporal variation of aerosol intensive parameters is much more pronounced on clean days than on polluted days. The strong temperature inversions more than doubled the peak values of diurnal half-hour average of aerosol absorption (i.e. $\beta_{abs\ clean}^{355\ nm}=18\,Mm^{-1}$, and $\beta_{abs\ polluted}^{355nm}=48\,Mm^{-1}$) and scattering (i.e. $\beta_{sca\ clean}^{355\ nm}=105\,Mm^{-1}$ and $\beta_{sca\ polluted}^{355nm}=210\,Mm^{-1}$). Organic species dominated the $PM_{2.5}$ component mass concentrations during the study periods; however, the lower values of AEAs suggest that the light absorbing particles did not arise due to light absorbing organic carbon or "brown carbon" during polluted days. The maximum scattering coefficient values on polluted days occurred 4 h later than the maximum scattering coefficient values on clean days, suggesting that formation of secondary organic aerosol is delayed by the strong temperature inversions during polluted days. The concurrent temporal maximum absorption coefficient values during clean and polluted days imply that traffic emissions are the dominant source of multispectral aerosol absorption. In general, SSAs are larger for all wavelengths on clean days (i.e. $SSA_{clean}^{355\ nm}=0.87$) than on polluted days (i.e. $SSA_{polluted}^{355\ nm}=0.83$). This can be attributed to restrictions on residential wood burning (source of primary organic aerosol) on polluted days.

T-matrix calculations (at 405 and 870 nm) illustrate that, as fractal aggregates become more and more compact, their SSA (AEA, AES) increases (decreases) even in the absence of other activities such as coating and mixing. The PA ambient measurements confirmed the similar variations of SSA, i.e. minimum in the morning rush hour for freshly emitted fractal-like chain aggregates and maximum on either side for aged and more compacted aggregates. However, derived D_f for laboratory generated kerosene soot from the T-matrix calculations of SSA, AEA, and AES are different from each other. Perhaps this is due to the use of the simplified model and identical RI for 405 and 870 nm to simulate light absorption and scattering by real soot containing complex particles, without considering coating and mixing and without exploring the

full parameter space for monomer diameter and number. Future work will take those issues into consideration.

Supplement related to this article is available online at:
http://www.atmos-chem-phys-discuss.net/11/25063/2011/
acpd-11-25063-2011-supplement.pdf.

References

Andreae, M. O. and Gelencsér, A.: Black carbon or brown carbon? The nature of light-absorbing carbonaceous aerosols, Atmos. Chem. Phys., 6, 3131–3148, doi:10.5194/acp-6-3131-2006, 2006.

Arnott, W. P., Moosmüller, H. and Walker, J.: Nitrogen dioxide and kerosene-flame soot calibration of photoacoustic instruments for measurement of light absorption by aerosols, Rev. Sci. Instrum., 71, 4545–4552, 2000.

Arnott, W. P., Zielinska, B., Rogers, C. F., Sagebiel, J., Park, K., Chow, J., Moosmüller, H., Watson, J. G., Kelly, K., Wagner, D., Sarofim, A., et al.: Evaluation of 1047-nm Photoacoustic Instruments and Photoelectric Aerosol Sensors in Source-Sampling of Black Carbon Aerosol and Particle-Bound PAHs from Gasoline and Diesel Powered Vehicles, Environ. Sci. Technol., 39, 5398–5406, 2005.

Arnott, W. P., Walker, J., Moosmüller, H., Elleman, R., Jonsson, H., Buzorius, G., Conant, W., Flagan, R., and Seinfeld, J.: Photoacoustic insight for aerosol light absorption aloft from meteorological aircraft and comparison with particle soot absorption photometer measurements: DOE Southern Great Plains climate research facility and the coastal stratocumulus imposed perturbation experiments, J. Geophys. Res., 111, D05S02, doi:10.1029/2005JD005964, 2006.

Barnard, J. C., Volkamer, R., and Kassianov, E. I.: Estimation of the mass absorption cross

Title Page

Abstract | Introduction

Conclusions | References

Tables | Figures

◄ | ►

◄ | ►

Back | Close

Full Screen / Esc

Printer-friendly Version

Interactive Discussion

section of the organic carbon component of aerosols in the Mexico City Metropolitan Area, Atmos. Chem. Phys., 8, 6665–6679, doi:10.5194/acp-8-6665-2008, 2008.

Bergstrom, R. W., Pilewskie, P., Russell, P. B., Redemann, J., Bond, T. C., Quinn, P. K., and Sierau, B.: Spectral absorption properties of atmospheric aerosols, Atmos. Chem. Phys., 7, 5937–5943, doi:10.5194/acp-7-5937-2007, 2007.

Bergstrom, R. W., Russell, P. B., and Hignett, P.: Wavelength Dependence of the Absorption of Black Carbon Particles: Predictions and Results from the TARFOX Experiment and Implications for the Aerosol Single Scattering Albedo, J. Atmos. Sci., 59, 567–577, 2002.

Bergstrom, R. W., Schmidt, K., Coddington, O., Pilewskie, P., Guan, H., Livingston, J., Redemann, J., and Russell, P. B.: Aerosol spectral absorption in the Mexico City area: results from airborne measurements during MILAGRO/INTEX B, Atmos. Chem. Phys., 10, 6333–6343, doi:10.5194/acp-10-6333-2010, 2010.

BGI: PQ100 Portable PM_{10}/TSP/$PM_{2.5}$. Prepared by BGI Incorporated, Waltham, MA, USA, http://www.bgiusa.com/aam/portable.htm, last accessed: 06/09/2011, 2009a.

BGI: PQ200 Ambient Fine Particulate Sampler, Prepared by BGI Incorporated, Waltham, MA, USA, http://www.bgiusa.com/aam/pq200.htm, last access: 06/09/2011, 2009b.

Bohren, C. F. and Huffman, D. R.: Absorption and Scattering of Light by Small Particles, John Wiley & Sons Inc., 530 pp., 1983.

Bond, T. C.: Spectral dependence of visible light absorption by carbonaceous particles emitted from coal combustion, Geophys. Res. Lett., 28, 4075-4078, 2001.

Bond, T. C. and Bergstrom, R. W.: Light absorption by carbonaceous particles: An investigative review, Aerosol Sci. Tech., 40, 27–67, 2006.

Chakrabarty, R. K., Moosmüller, H., Arnott, W. P., Garro, M. A., and Walker, J.: Structural and fractal properties of particles emitted from spark ignition engines, Environ. Sci. Technol., 40, 6647–6654, doi:10.1021/es060537y, 2006.

Chakrabarty, R. K., Moosmüller, H., Chen, L.-W. A., Lewis, K., Arnott, W. P., Mazzoleni, C., Dubey, M. K., Wold, C. E., Hao, W. M., and Kreidenweis, S. M.: Brown carbon in tar balls from smoldering biomass combustion, Atmos. Chem. Phys., 10, 6363–6370, doi:10.5194/acp-10-6363-2010, 2010.

Chen, C.-L., Tsuang, B.-J., Tu, C.-Y., Cheng, W.-L., and Lin, M.-D.: Wintertime vertical profiles of air pollutants over a suburban area in central Taiwan, Atmos. Environ, 36, 2049–2059, 2002.

Chen, L.-W. A., Verburg, P., Shackelford, A., Zhu, D., Susfalk, R., Chow, J. C., and Watson,

Photoacoustic optical properties

M. Gyawali et al.

Title Page

Abstract	Introduction
Conclusions	References
Tables	Figures

◄   ►❘

◄   ►

Back   Close

Full Screen / Esc

Printer-friendly Version

Interactive Discussion

J. G.: Moisture effects on carbon and nitrogen emission from burning of wildland biomass, Atmos. Chem. Phys., 10, 6617–6625, doi:10.5194/acp-10-6617-2010, 2010.

Chow, J. C., Watson, J. G.: Lowenthal, D. H., Chen, L.-W. A., Tropp, R. J., Park, K., Magliano, K. L.: $PM_{2.5}$ and PM_{10} mass measurements in California's San Joaquin Valley, Aerosol Sci. Technol., 40(10), 796–810, 2006.

Clarke, A. D., Noone, K. J., Heintzenberg, J., Warren, S. G., and Covert, D. S.: Aerosol light absorption measurement techniques: Analysis and intercomparisons, Atmos. Environ., 21, 1455–1465, doi:10.1016/0004-6981(67)90093-5, 1987.

Corr, C., Krotkov, N., Madronich, S., Slusser, J., Holben, B., Gao, W., Flynn, J., Lefer, B., and Kreidenweis, S.: Retrieval of aerosol single scattering albedo at ultraviolet wavelengths at the T1 site during MILAGRO, Atmos. Chem. Phys., 9, 5813–5827, doi:10.5194/acp-9-5813-2009, 2009.

D'Alessio, A., D'Anna, A., Gambi, G., and Minutolo, P.: The spectroscopic characterisation of UV absorbing nanoparticles in fuel rich soot forming flames, J. Aerosol Sci., 29, 397–409, 1998.

Dubovik, O., Holben, B., Eck, T. F., Smirnov, A., Kaufman, Y., King, M. D., Tanre, D., and Slutsker, I.: Variability of absorption and optical properties of key aerosol types observed in worldwide locations, J. Atmos. Sci., 59, 590–608, 2002.

Eck, T. F., Holben, B. N., Reid, J. S., Dubovik, O., Smirnov, A., O'Neill, N. T., Slutsker, I., and Kinne, S.: Wavelength dependence of the optical depth of biomass burning, urban, and desert dust aerosols, J. Geophys. Res., 104, D24, 31333–31349, 1999.

Flowers, B. A., Dubey, M. K., Mazzoleni, C., Stone, E. A., Schauer, J. J., Kim, S.-W., and Yoon, S. C.: Optical-chemical-microphysical relationships and closure studies for mixed carbonaceous aerosols observed at Jeju Island; 3-laser photoacoustic spectrometer, particle sizing, and filter analysis, Atmos. Chem. Phys., 10, 10387–10398, doi:10.5194/acp-10-10387-2010, 2010.

Grisdale, R. O.: The formation of black carbon, *J. Appl. Phys*, 24, doi:10.1063/1.1721452, 1953.

Gyawali, M., Arnott, W. P., Lewis, K., and Moosmüller, H.: In situ aerosol optics in Reno, NV, USA during and after the summer 2008 California wildfires and the influence of absorbing and non-absorbing organic coatings on spectral light absorption, Atmos. Chem. Phys., 9, 8007–8015, doi:10.5194/acp-9-8007-2009, 2009.

Hansen, J., Johnson, D., Lacis, A., Lebedeff, S., Lee, P., Rind, D. and Russell, G.:

Photoacoustic optical properties

M. Gyawali et al.

Title Page

Abstract	Introduction
Conclusions	References
Tables	Figures

|◄ | ►|

◄ | ►

Back | Close

Full Screen / Esc

Printer-friendly Version

Interactive Discussion

Climate Impact of Increasing Atmospheric Carbon Dioxide, Science, 213, 957-966, doi:10.1126/science.213.4511.957, 1981.

Hofzumahaus, A., Kraus, A., Kylling, A., and Zerefos, C. S.: Solar actinic radiation (280–420 nm) in the cloud-free troposphere between ground and 12 km altitude: Measurements and model results, J. Geophys. Res., 107, 8139, doi:200210.1029/2001JD900142, 2002.

Horvath, H.: Atmospheric light absorption–A review, Atmos. Environ., 27, 293–317, 1993.

Huang, C. H. and Tai, C. Y.: Relative humidity effect on $PM_{2.5}$ readings recorded by collocated beta attenuation monitors. Environmental Engineering Science, 25(7), 1079–1089. ISI:000259125600013, 2008.

Jacobson, M. C., Hansson, H.-C., Noone, K. J., and Charlson, R. J.: Organic atmospheric aerosols: Review and state of the science, Rev. Geophys., 38, 267–294, 2000.

Jacobson, M. Z.: Isolating nitrated and aromatic aerosols and nitrated aromatic gases as sources of ultraviolet light absorption, J. Geophys. Res., 104, 3527–3542, 1999.

Janhäll, S., Olofson, K. F. G., Andersson, P. U., Pettersson, J. B. C., and Hallquist, M.: Evolution of the urban aerosol during winter temperature inversion episodes, Atmos. Environ., 40, 5355–5366, doi:10.1016/j.atmosenv.2006.04.051, 2006.

Ji, X., Le Bihan, O., Ramalho, O., Mandin, C., D'Anna, B., Martinon, L., Nicolas, M., Bard, D., and Pairon, J.-C.: Characterization of particles emitted by incense burning in an experimental house, Ind. Air, 20, 147–158, doi:10.1111/j.1600-0668.2009.00634.x, 2010.

Kikas, U., Reinart, A., Vaht, M., and Veismann, U.: A case study of the impact of boundary layer aerosol size distribution on the surface UV irradiance, Atmos. Environ., 35, 5041–5051, 2001.

Kirchstetter, T. W., Novakov, T., and Hobbs, P. V.: Evidence that the spectral dependence of light absorption by aerosols is affected by organic carbon, J. Geophys. Res., 109, D21208, doi:10.1029/2004JD004999, 2004.

Lack, D. A. and Cappa, C. D.: Impact of brown and clear carbon on light absorption enhancement, single scatter albedo and absorption wavelength dependence of black carbon, Atmos. Chem. Phys., 10, 4207–4220, doi:10.5194/acp-10-4207-2010, 2010.

Lack, D. A., Cappa, C. D., Cross, E. S., Massoli, P., Adam T. Ahern, A. T., Davidovits, P., and Onasch, T. B.: Absorption Enhancement of Coated Absorbing Aerosols: Validation of the Photo Acoustic Technique for Measuring the Enhancement, Aerosol Sci. Technol., 43, 1006–1012, 2009.

Levoni, C., Cervino, M., Guzzi, R., and Torricella, F.: Atmospheric aerosol optical properties:

Photoacoustic optical properties

M. Gyawali et al.

Title Page

Abstract | Introduction

Conclusions | References

Tables | Figures

◄ | ►

Back | Close

Full Screen / Esc

Printer-friendly Version

Interactive Discussion

a database of radiative characteristics for different components and classes, Appl. Opt., 36, 8031–8041, 1997.

Lewis, K., Arnott, W. P., Moosmüller, H., and Wold, C. E.: Strong spectral variation of biomass smoke light absorption and single scattering albedo observed with a novel dual-wavelength photoacoustic instrument, J. Geophys. Res., 113, D16203, doi:10.1029/2007JD009699, 2008.

Lewis, K. A., Arnott, W. P, Moosmüller, H., Chakrabarty, R. K., Carrico, C. M, Kreidenweis, S. M., Day, D. E., Malm, W. C., Laskin, A., Jimenez, J. L.,Ulbrich, I. M. Huffman, J. A., Onasch, T. B.,Trimborn, A., Lui, L., and Mishchenko, M. I.: Reduction in Biomass Burning Aerosol Light Absorption upon Humidification: Roles of Inorganically-Induced Hygroscopicity, Particle Collapse, and Photoacoustic Heat and Mass Transfer, Atmos. Chem. Phys., 9, 8949–8966, doi:10.5194/acp-9-8949-2009, 2009.

Liu, L., Mishchenko, M. I., and Arnott, W. P.: A study of radiative properties of fractal soot aggregates using the superposition T-matrix method, J. Quant. Spectrosc. Ra., 109, 2656–2663, 2008.

Mackowski, D. W.: A simplified model to predict the effects of aggregation on the absorption properties of soot particles, J. Quant. Spectrosc. Ra., 100, 237–249, 2006.

Mackowski, D. W. and Mishchenko, M. I.: Calculation of the T matrix and the scattering matrix for ensembles of spheres, J. Opt. Soc. Am. A, 13, 2266–2278, doi:10.1364/JOSAA.13.002266, 1996.

Martins, J. V., Artaxo, P., Kaufman, Y. J., Castanho, A. D., and Remer, L. A.: Spectral absorption properties of aerosol particles from 350–2500 nm, Geophys. Res. Lett., 36, L13810, doi:200910.1029/2009GL037435, 2009.

Mishchenko, M. I., Travis, L., and Mackowski, D. W.: T-matrix computations of light scattering by non spherical particles: A review, J. Quant. Spectrosc. Rad., 55, 535–575, 1996.

Moosmüller, H. and Arnott, W. P.: Particle Optics in the Rayleigh Regime. J. Air Waste Manage. Assoc., 59, 1028–1031, 2009.

Moosmüller, H. and Chakrabarty, R. K.: Technical Note: Simple analytical relationships between Ångström coefficients of aerosol extinction, scattering, absorption, and single scattering albedo, Atmos. Chem. Phys. Discuss., 11, 19213–19222, doi:10.5194/acpd-11-19213-2011, 2011.

Moosmüller, H., Chakrabarty, R. K., Ehlers, K. M., and Arnott, W. P.: Absorption Ångström coefficient, brown carbon, and aerosols: basic concepts, bulk matter, and spherical particles,

Atmos. Chem. Phys., 11, 1217–1225, doi:10.5194/acp-11-1217-2011, 2011.

Moosmüller, H., Chakrabarty, R. K., and Arnott, W. P.: Aerosol light absorption and its measurement: A review, J. Quant. Spectrosc. Radiat. Trans., 110, 844–878, 2009.

Paredes-Miranda, G., Arnott, W. P., Jimenez, J. L., Aiken, A. C., Gaffney, J. S., and Marley, N. A.: Primary and secondary contributions to aerosol light scattering and absorption in Mexico City during the MILAGRO 2006 campaign, Atmos. Chem. Phys., 9, 3721–3730, doi:10.5194/acp-9-3721-2009, 2009.

Petzold, A. and Schönlinner, M.: Multi-angle absorption photometry–a new method for the measurement of aerosol light absorption and atmospheric black carbon, J. Aerosol Sci., 35, 421–441, 2004.

Reid, J. S., Hobbs, P. V., Ferek, R. J., Blake, D. R., Martins, J. V., Dunlap, M. R., and Liousse, C.: Physical, chemical, and optical properties of regional hazes dominated by smoke in Brazil, J. Geophys. Res., 103, 32059–32080, 1998.

Reid, J. S., Eck, T., Christopher, S., Hobbs, P. V., and Holben, B. N.: Use of the Angstrom exponent to estimate the variability of optical and physical properties of aging smoke particles in Brazil, J. Geophys. Res., 104, 27473–27489, 1999.

Reuder, J. and Schwander, H.: Aerosol effects on UV radiation in nonurban regions, J. Geophys. Res., 104, 4065–4077, 1999.

Roden, C. A., Bond, T. C., Conway, S., Benjamin, A., and Pinel, A. B. O.: Emission factors and real-time optical properties of particles emitted from traditional wood burning cookstoves, Environ. Sci. Technol., 40, 6750–6757, 2006.

Schuster, G. L., Dubovik, O., and Holben, B. N.: Angstrom exponent and bimodal aerosol size distributions, J. Geophys. Res., 111, D07207, doi:10.1029/2005JD006328, 2006.

Schwab, J. J., Felton, H. D., Rattigan, O. V., and Demerjian, K. L.: New York state urban and rural measurements of continuous $PM_{2.5}$ mass by FDMS, TEOM, and BAM, J. Air Waste Manage. Assoc., 56(4), 372–383, 2006.

Seinfeld, J. H. and Pandis, S. N.: Atmospheric Chemistry and Physics: From Air Pollution to Climate Change, 2nd ed., Wiley, Hoboken, NJ, USA, 2006.

Sheridan, P., Arnott, W. P., Ogren, J., Andrews, E., Atkinson, D., Covert, D., Moosmüller, H., Petzold, A., Schmid, B., Strawa, A., Varma, R., and Virkkula, A.: The Reno Aerosol Optics Study: An evaluation of aerosol absorption measurement methods, Aerosol Sci. Tech., 39, 1–16, doi:10.1080/027868290901891, 2005.

Silva, P., Vawdrey, E., Corbett, M., and Erupe, M.: Fine particle concentrations and compo-

sition during wintertime inversions in Logan, Utah, USA, Atmos. Environ., 41, 5410–5422, doi:10.1016/j.atmosenv.2007.02.016, 2007.

Sokolik, I. and Toon, O.: Incorporation of mineralogical composition into models of the radiative properties of mineral aerosol from UV to IR wavelengths, J. Geophys. Res., 104, 9423–9444, 1999.

Sorensen, C. M.: Light scattering by fractal aggregates: A review, Aerosol Sci. Tech., 35, 648–687, 2001.

Sorensen, C. M. and G. C. Roberts.: The Prefactor of Fractal Aggregates, J. Colloid Interface Sci., 186, 447–452, 1997.

Stephens, S., Madronich, S., Wu, F., Olson, J.B., Ramos, R., Retama, A., and Munoz, R.: Weekly patterns of Mexico City's surface concentrations of CO, NOx, PM_{10} and O_3 during 1986–2007, Atmos. Chem. Phys., 8, 5313–5325, 2008, http://www.atmos-chem-phys.net/8/5313/2008/.

Sun, H., Biedermann, L., and Bond, T.: Color of brown carbon: A model for ultraviolet and visible light absorption by organic carbon aerosol, Geophys. Res. Lett., 34, L17813, doi:10.1029/2007GL029797, 2007.

Taylor, T., L'Ecuyer, T., Slusser, J., Stephens, G., and Goering, C.: An operational retrieval algorithm for determining aerosol optical properties in the ultraviolet, J. Geophys. Res., 113, D03201, doi:10.1029/2007JD008661, 2008.

van de Hulst, H. C.: Light Scattering by Small Particles, Dover Publications, Inc., New York, USA, 453 pp., 1981.

Watson, J. G., Chow, J. C., Lowenthal, D. H., and Magliano, K. L.: Estimating aerosol light scattering at the Fresno Supersite, Atmos. Environ., 42, 1186–1196, 2008.

Watson, J. G. and Chow, J. C: A wintertime $PM_{2.5}$ episode at the Fresno, CA, supersite, Atmos. Environ, 36(3), 465–475, 2002.

Wentzel, M., Gorzawski, H., Naumann, K., Saathoff, H., and Weinbruch, S.: Transmission electron microscopical and aerosol dynamical characterization of soot aerosols, J. Aerosol Sci., 34, 1347–1370, 2003.

Yang, C., Lin, T., and Chang, F.: Particle size distribution and PAH concentrations of incense smoke in a combustion chamber, Environmental Pollution, 145, 606–615, doi:10.1016/j.envpol.2005.10.036, 2007.

Zaveri, R. A., Berkowitz, C. M., Brechtel, F. J., Gilles, M. K., Hubbe, J. M., Jayne, J. T., Kleinman, L. I., Laskin, A., Madronich, S., Onasch, T. B., Pekour, M. S., Springston, S. R., Thornton,

J. A., Tivanski, A. V., and Worsnop, D. R.: Nighttime chemical evolution of aerosol and trace gases in a power plant plume: Implications for secondary organic nitrate and organosulfate aerosol formation, NO_3 radical chemistry, and N_2O_5 heterogeneous hydrolysis, J. Geophys. Res., 115, D12304, doi:10.1029/2009JD013250, 2010.
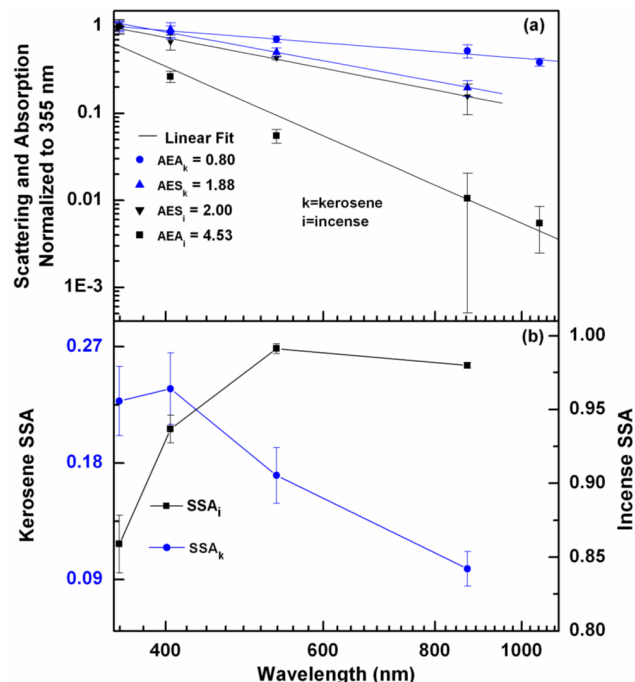
Fig. 1. Intensive aerosol optical properties for kerosene and incense smoke. Ångström exponents of **(a)** scattering (AES) and absorption (AEA), where error bars indicate the standard deviation of the mean and **(b)** single scattering albedo (SSA). Uncertainty on SSA was determined by assuming 5 % relative uncertainty in photoacoustic absorption coefficient measurements and 15 % relative uncertainty in scattering coefficient measurements.
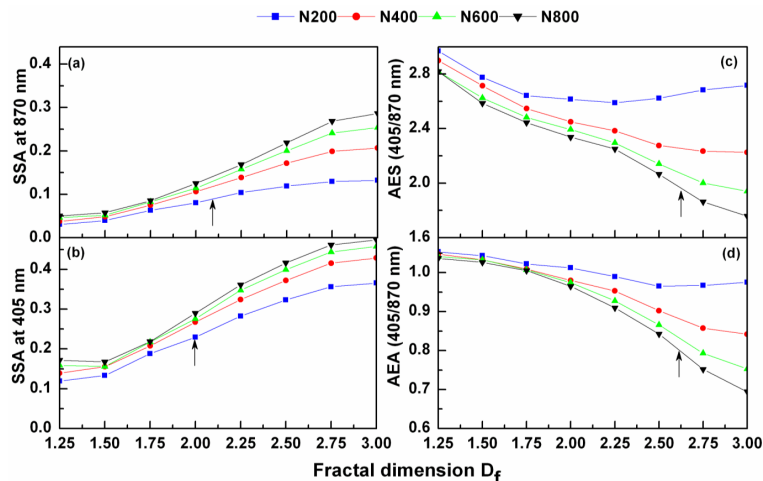
Fig. 2. T-matrix calculations of SSA at **(a)** 870 nm and **(b)** 405 nm, as well as Ångström exponents of **(c)** scattering (AES) and **(d)** absorption (AEA) versus fractal dimension (D_f) for different number of monomers (N). The arrows are for laboratory measurements. The monomer radius is 15 nm and refractive indices at both wavelengths are 1.75 + I 0.5.

Discussion Paper | Discussion Paper | Discussion Paper | Discussion Paper | Discussion Paper

ACPD

11, 25063–25098, 2011

Photoacoustic optical properties

M. Gyawali et al.

Title Page

Abstract | Introduction

Conclusions | References

Tables | Figures

|◄ | ►|

◄ | ►

Back | Close

Full Screen / Esc

Printer-friendly Version

Interactive Discussion
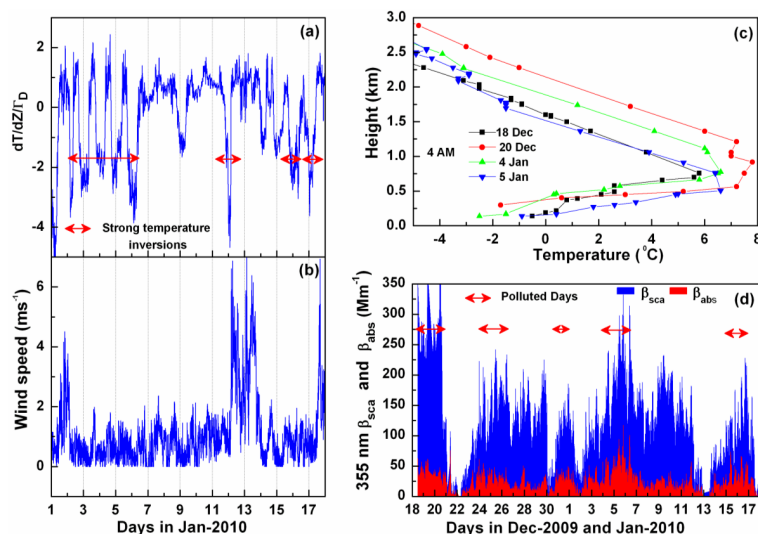
Fig. 3. Meteorology and aerosol optics measurements at 355 nm during winter 2009/2010 at Reno, Nevada. **(a)** Temperature gradient normalized to dry adiabatic lapse rate (−9.8 °C), with negative values indicating temperature inversions. **(b)** wind speed, **(c)** temperature profiles from radiosonde launches, whereas the height is above the ground level (a.g.l.). Strong temperature inversions are associated with the highly polluted events of the winter season, **(d)** two minute average of the ambient aerosol scattering and absorption coefficients.
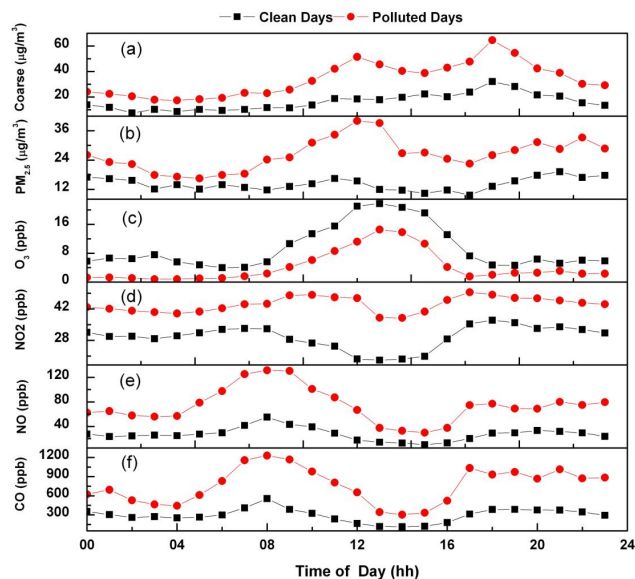
Fig. 4. Diurnal variation of hourly average concentrations of **(a)** coarse particles, **(b)** PM$_{2.5}$, **(c)** ozone, **(d)** nitrogen oxide, **(e)** nitrogen dioxide, and **(f)** carbon monoxide.
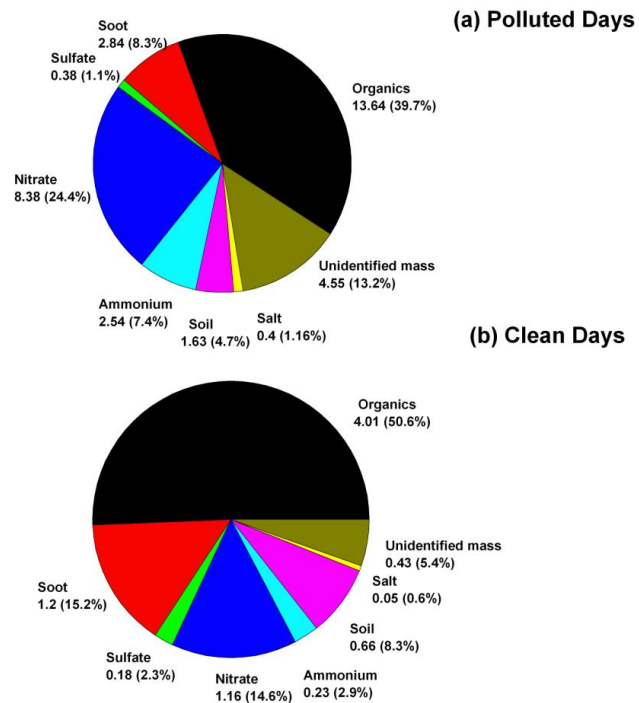
Fig. 5. Twenty-four-hour average PM$_{2.5}$ component concentrations (μg m^{-3}) for **(a)** polluted days (18 and 24 December, and 5 January) and **(b)** clean days (21 December, and 14 and 17 January).

Title Page

Abstract | Introduction

Conclusions | References

Tables | Figures

◄ | ►

◄ | ►

Back | Close

Full Screen / Esc

Printer-friendly Version

Interactive Discussion

Full Screen / Esc
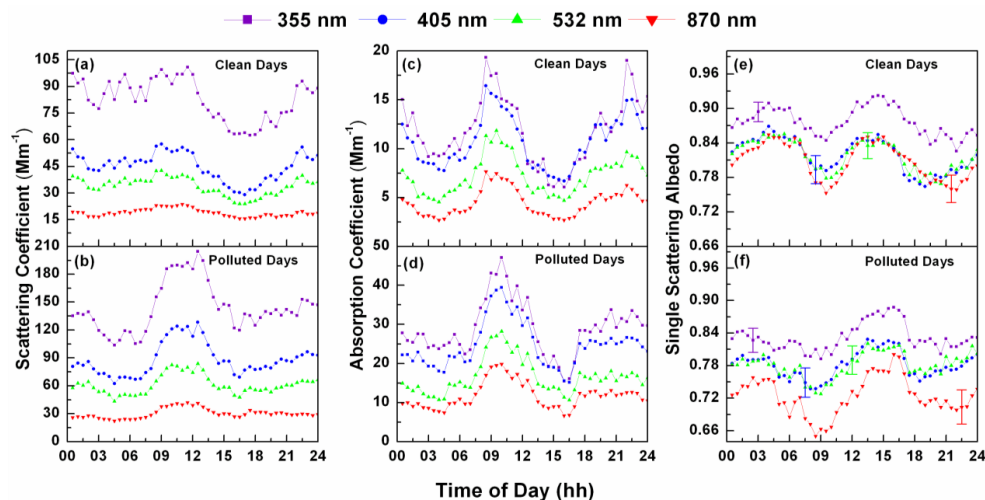
Fig. 6. Diurnal variation of half-hour average ambient aerosol optical properties from 18 December 2009 to 18 January 2010 at wavelengths 355, 405, 532, and 870 nm for clean and polluted days. **(a)** and **(b)** are the scattering coefficients, **(c)** and **(d)** are the absorption coefficients, and **(e)** and **(f)** are the single scattering albedo (SSA). Uncertainty on SSA was determined by assuming 5 % relative uncertainty in photoacoustic absorption coefficient measurements and 15 % relative uncertainty in scattering coefficient measurements.
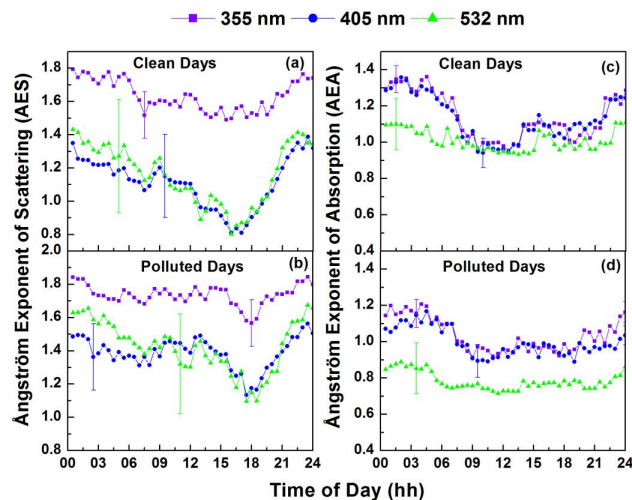
Fig. 7. Diurnal variation of half-hour average ambient intensive aerosol optical properties for clean and polluted days from 18 December 2009 to 18 January 2010 at wavelengths 355, 405, and 532 nm using 870 nm as a reference. **(a)** and **(b)** Ångström exponent of scattering (AES), **(c)** and **(d)** Ångström exponent of absorption (AEA). Uncertainty on AES and AEA were determined by assuming 5 % relative uncertainty in photoacoustic absorption coefficient measurements and 15 % relative uncertainty in scattering coefficient measurements.
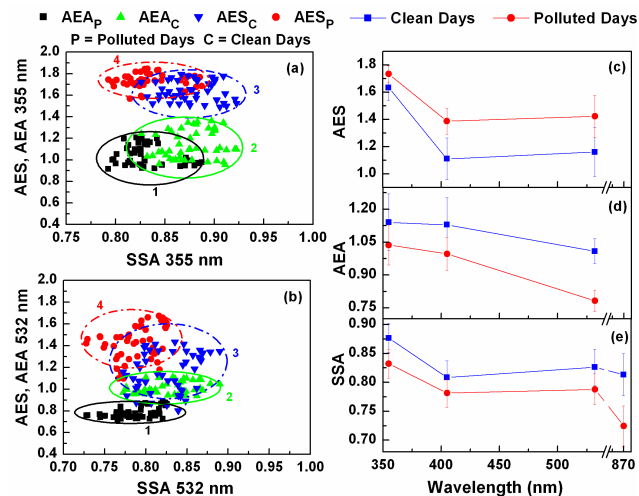
Fig. 8. Ambient intensive aerosol optical properties from 18 December 2009 to 18 January 2010. Half-hour average AES and AEA versus single scattering albedo (SSA) for **(a)** 355 nm and **(b)** 532 nm. Averaged **(c)** AES and **(d)** AEA for "clean days" and "polluted days" using 870 nm as a reference wavelength. **(e)** similar plot for SSA.